Materials Today Communications 48 (2025) 113325

Contents lists available at ScienceDirect

Materials Today Communications

journal homepage: www.elsevier.com/locate/mtcomm

Modeling for homogeneous Mg electrodeposition on Mg metal negative electrode in rechargeable Mg batteries

Atsushi Tamura [a], Toshihiko Mandai [b], Shunsuke Yagi [a,*]

[a] Institute of Industrial Science, The University of Tokyo, 4-6-1 Komaba, Meguro-ku, Tokyo 153-8505, Japan
[b] Research Center for Energy and Environmental Materials, National Institute for Materials Science (NIMS), 1-1 Namiki, Tsukuba, Ibaraki 305-0044, Japan

ARTICLE INFO

Keywords:
Diffusion
Flux
Surface morphology
Electrodeposition
Mg battery

ABSTRACT

Rechargeable Mg batteries have received intense attention as affordable rechargeable batteries with high electromotive force, energy density, and safety. Achieving uniform dissolution and electrodeposition of Mg metal negative electrode is vital for the development of rechargeable Mg batteries. This study investigates the behavior of Mg electrodeposition on non-uniform Mg metal surfaces formed through several discharge/charge cycles using simulations based on the Newman model followed by experimental validation. The simulations revealed that the surface morphology of the Mg metal negative electrode affected the distribution of the Mg^{2+} ion concentration, flux, and current density in the electrolyte. Uniform electrodeposition can be achieved by maintaining a higher concentration of Mg^{2+} ions in the pits formed on the surface, for example by ensuring a higher Mg^{2+} ion diffusion coefficient, a smaller current density, and larger but shallower pits. The experimental results support these findings, providing a strategy to achieve uniform Mg electrodeposition and optimal design of the electrolyte.

1. Introduction

Due to their high energy density, lithium-ion batteries (LIBs) are widely used in a variety of products such as mobile phones. Currently, carbonaceous negative electrodes (372 mAh g^{-1}) are used in LIBs, where charging and discharging occur through the intercalation and deintercalation of Li^+ ions. While much higher energy density and capacity (3860 mAh g^{-1}) can be achieved by replacing carbonaceous negative electrodes with Li metal negative electrodes, the use of Li metal negative electrodes poses challenges such as dendrite growth during charging which leads to short circuits caused by the piercing of the separator by the dendrites and/or capacity loss due to Li flaking [1,2].

In recent years, there has been considerable interest in rechargeable batteries that use negative electrodes based on metals other than Li such as Mg, Ca, and Al. Among these, Mg is one of the most promising candidate metals for metal negative electrodes [3,4]. Previous studies have reported that dendrite growth rarely occurs during charging of rechargeable Mg batteries (RMBs) [5,6]. RMBs have advantages of the high capacity of the Mg metal negative electrode (2200 mAh g^{-1}) and low standard electrode potential of Mg (−2.36 V *vs.* SHE) [7] allowing a higher electromotive force.

The first demonstration of RMBs was reported by Aurbach et al., who used Chevrel phase Mo_6S_8 as the positive electrode [8]. This battery exhibited excellent cycling characteristics but suffered from low cell voltage and capacity (1.1–1.2 V, 75 mAh g^{-1}) [8,9]. Therefore, recent research has focused on improving positive electrode materials, particularly for oxides that generally have higher redox potentials, such as spinel $MgMn_2O_4$ (~2.9 V *vs.* Mg/Mg^{2+}, 180 mAh g^{-1}) [10–12], $MgCoSiO_4$ (~1.5 V *vs.* Mg/Mg^{2+}, 250 mAh g^{-1}) [13], and a-MnO_2 (~2.5 V *vs.* Mg/Mg^{2+}, 220 mAh g^{-1}) [14].

By contrast, research on the negative electrode has been relatively limited. Because RMBs are repeatedly discharged and charged during use, the Mg metal negative electrode undergoes dissolution and electrodeposition many times, eventually leading to electrodeposition on an uneven and rough Mg surface. Understanding the Mg^{2+} concentration distribution in the electrolyte and the current density on the electrode surface is essential for analyzing this phenomenon and for obtaining a flat Mg surface. However, it is difficult to obtain these properties experimentally. Therefore, in the present study, these physical properties are investigated by building models based on the Newman model incorporating concentrated electrolyte theory and porous electrode theory. The models are implemented using the COMSOL Multiphysics® software. While many cell simulations have been performed for LIBs [15–22], the characteristics of the Mg^{2+} ion transport in the cell remain

* Corresponding author.
E-mail address: syagi@iis.u-tokyo.ac.jp (S. Yagi).

https://doi.org/10.1016/j.mtcomm.2025.113325
Received 14 May 2025; Received in revised form 5 July 2025; Accepted 14 July 2025
Available online 14 July 2025

unclear, and only a few simulation studies have been reported [23]. To ensure that the simulations are relevant to practical devices, they were performed using the 3D structure of a laminated cell. The Mg^{2+} ion concentration distribution in the electrolyte and the current density on the electrode surface were estimated and compared with the experimental results to develop a strategy for achieving uniform Mg electrodeposition.

2. Governing equations

In this study, the following diffusion equation, similar to the Stefan-Maxwell equation generally used for gas diffusion [24], was considered based on the interaction among the dissociated ions and solvent molecules [21,25–29]:

$$-c_i\nabla\overline{\mu}_i=\sum\nolimits_j K_{ij}(\mathbf{v_i}-\mathbf{v_j})=RT\sum\nolimits_j\frac{c_ic_j}{c_T\mathfrak{D}_{ij}}(\mathbf{v_i}-\mathbf{v_j}) \tag{1}$$

where c_i is the concentration of the dissociated ions or solvent molecules i, c_T is defined as $c_T=\sum_i c_i$, including solvents, $\overline{\mu}_i$ is the electrochemical potential of species i, K_{ij} is the coefficient of friction between species i and j, $\mathbf{v_i}$ is the velocity of species i, R is the gas constant, T is the temperature, and $\mathfrak{D}_{ij}$ is the diffusion coefficient for interaction of species i and j. The relationship between K_{ij} and $\mathfrak{D}_{ij}$ is given by:

$$K_{ij}=\frac{RTc_ic_j}{c_T\mathfrak{D}_{ij}} \tag{2}$$

According to Newton's third law, that is the law of action and reaction,

$$K_{ij}=K_{ji} \tag{3}$$

and thus, we obtain the following equation:

$$\mathfrak{D}_{ij}=\mathfrak{D}_{ji} \tag{4}$$

Three types of substances were considered, namely cations, anions, and solvents, with one species of each type. In this case, Eq. 1 can be written with the cation and anion species denoted by the subscripts + and −, respectively, to obtain:

$$-c_+\nabla\overline{\mu}_+=K_{+0}(\mathbf{v}_+-\mathbf{v_0})+K_{+-}(\mathbf{v}_+-\mathbf{v}_-) \tag{5}$$

$$-c_-\nabla\overline{\mu}_-=K_{-0}(\mathbf{v}_--\mathbf{v_0})+K_{-+}(\mathbf{v}_--\mathbf{v}_+) \tag{6}$$

By summing Eqs. 5 and 6, and considering Eq. 3, the following equation is obtained:

$$c\nabla\overline{\mu}_{el}=K_{0+}(\mathbf{v_0}-\mathbf{v}_+)+K_{0-}(\mathbf{v_0}-\mathbf{v}_-) \tag{7}$$

where $\overline{\mu}_{el}$ is the electrochemical potential of the electrolyte, $\overline{\mu}_{el}=\nu_+\overline{\mu}_+ + \nu_-\overline{\mu}_-$, and ν_+ and ν_- are the numbers of cations and anions formed by the dissociation of a single electrolyte molecule [25]. Therefore, the relationship between the molar concentration of single electrolyte c and c_+ and c_- is naturally derived as $c=\frac{c_+}{\nu_+}=\frac{c_-}{\nu_-}$. Because the current can be considered as the flux of particles carrying a charge, the current density $\mathbf{i}$ is expressed by the following equation:

$$\mathbf{i}=\sum_i z_iF\mathbf{N_i} \tag{8}$$

where z_i is the charge of species i, F is the Faraday constant, and $\mathbf{N_i}$ is the flux of species i. In addition, because the electrolyte must satisfy electrical-neutrality conditions, the following equation holds:

$$\sum_i z_ic_i=0 \tag{9}$$

The flux of cations $\mathbf{N}_+$ can be described as a linear combination of diffusion and migration as follows:

$$\mathbf{N}_+=c_+\mathbf{v}_+=-\frac{\nu_+\mathfrak{D}}{\nu RT}\frac{c_T}{c_0}c\nabla\overline{\mu}_{el}+\frac{t_+^0}{z_+F}\mathbf{i}+c_+\mathbf{v_0} \tag{10}$$

where $\nu=\nu_++\nu_-$, t_+^0 is the cation transference number with respect to the velocity of solvent, and $\mathfrak{D}$ is the diffusion coefficient based on the thermodynamic driving force which is expressed by following equation:

$$\mathfrak{D}=\frac{\mathfrak{D}_{0+}\mathfrak{D}_{0-}(z_+-z_-)}{z_+\mathfrak{D}_{0+}-z_-\mathfrak{D}_{0-}} \tag{11}$$

Eq. 10 includes three terms on the right-hand side, corresponding to diffusion, migration, and reference flux, respectively. However, the first term contains the gradient of the electrochemical potential and the diffusion coefficient based on the thermodynamic driving force, which are difficult to measure and should be avoided in physical simulations. Therefore, the first term is instead expressed using the diffusion coefficient D based on Fick's law as follows:

$$\frac{\mathfrak{D}}{\nu RT}\frac{c_T}{c_0}c\nabla\overline{\mu}_{el}=D\left(1-\frac{d\ln c_0}{d\ln c}\right)\nabla c \tag{12}$$

By substituting the first term of Eq. 10 into Eq. 12, Eq. 13 is obtained based on the concentration gradient.

$$\mathbf{N}_+=-\nu_+D\left(1-\frac{d\ln c_0}{d\ln c}\right)\nabla c+\frac{t_+^0}{z_+F}\mathbf{i}+c_+\mathbf{v_0} \tag{13}$$

The distribution of current density $\mathbf{i}$ in the solution is determined using the following procedure. We introduce a suitable reference electrode at a point in the solution measured with respect to a reference electrode at a fixed point. The general expression for the reactions at the reference electrode is as follows:

$$s_-M_-^{z_-}+s_+M_+^{z_+}+s_0M_0^{z_0}\rightleftharpoons ne^- \tag{14}$$

where s_i is the stoichiometric reaction coefficient of species i, M_i is the chemical formula of species i, and n is the number of electrons involved in the electrode reaction. According to reaction 14, because the chemical potential of the electron in the electrode made of the same material is the same, the balance of the gradients of the electrochemical potentials and electric potential Φ of the reference electrode is expressed as follows:

$$s_-\nabla\overline{\mu}_-+s_+\nabla\overline{\mu}_++s_0\nabla\overline{\mu}_0=-nF\nabla\Phi \tag{15}$$

The left-hand side of this equation can be rearranged using Eq. 7 to obtain an expression for $\nabla\overline{\mu}_{el}$. Considering the Gibbs-Duhem equation and using Eq. 12, a generalized current density equation was obtained that relates the measurable diffusion coefficient and the thermodynamic diffusion coefficient, and the electrochemical potential gradient and the concentration gradient, as follows:

$$\mathbf{i}=-\kappa\nabla\Phi-\frac{\nu\kappa RT}{F}\left(\frac{s_+}{n\nu_+}+\frac{t_+^0}{z_+\nu_+}-\frac{s_0c}{nc_0}\right)\left(1+\frac{d\ln f_{+-}}{d\ln c}\right)\nabla\ln c \tag{16}$$

where κ is the conductivity and f_{+-} is the mean molar activity coefficient of the electrolyte. It should be noted that the following relationship between the measurable diffusion coefficient D and the thermodynamic diffusion coefficient $\mathfrak{D}$ is used [25].

$$D=\mathfrak{D}\frac{c_T}{c_0}\left(1+\frac{d\ln f_{+-}}{d\ln c}\right) \tag{17}$$

In this study, Eqs. 13 and 16 were used for the physical simulation of MRBs. The electrolyte (Mg salt) used in this study is $Mg[Al(HFIP)_4]_2$, which dissociates into one Mg^{2+} ion and two $[Al(HFIP)_4]^-$ ions. Therefore, $z_+=2$, $\nu_+=1$, and $\nu=\nu_++\nu_-=3$. Two electrons participate in the electrode reaction, namely Mg electrodeposition, and $s_+=-1, s_-=0$, and $s_0=0$. When the above values are substituted into Eqs. 13 and 16, and $\mathbf{v_0}$ is assumed to be zero, the following Eqs. 18 and 19, can be obtained for the flux and current density in the RMBs, respectively:

$$\mathbf{N}_+ = -D\nabla c + \frac{\mathbf{i}t_+^0}{2F} \tag{18}$$

$$\mathbf{i} = -\kappa\nabla\Phi + \frac{3\kappa RT}{2F}\left(1-t_+^0\right)\left(1+\frac{d\ln f_{+-}}{d\ln c}\right)\nabla\ln c \tag{19}$$

Let us then assume that the current density i on the surface of the Mg negative electrode obeys the Butler-Volmer equation:

$$i = i_0\left\{\exp\left(\frac{2\alpha_a F\eta}{RT}\right) - \exp\left(-\frac{2\alpha_c F\eta}{RT}\right)\right\} \tag{20}$$

where i_0 is the exchange current density, α_a and α_c are the charge transfer coefficients, F is the Faraday constant, η is the overpotential, and R is the gas constant. It should be noted that the ratio of the ion concentration in the bulk and at the electrode surface is assumed to be 1, and the coefficient inside the parentheses of the exponential function is 2 because Mg electrodeposition is a two-electron reaction. The overpotential is defined using the following equation:

$$\eta = \phi_s - \phi_l - E_{OCP} \tag{21}$$

where ϕ_s is the solid-phase potential, ϕ_l is the liquid-phase potential, and E_{OCP} is the open-circuit potential. The equation for Mg^{2+} ion diffusion in the electrolyte solution soaked in the composite positive electrode and other related equations used in the calculations are provided in the Supporting Information.

3. Experimental

COMSOL Multiphysics® 6.2 software was used to perform simulations based on the equations discussed in the previous section. This simulation assumes solvent velocity $\mathbf{v_0} = 0$ and does not consider the effect of convection on ion transport. This assumption is valid under static electrolyte and relatively low current density conditions considered in this paper but needs to be corrected in conjunction with convection effects under high rate or high temperature conditions. Due to the scarcity of available data for Mg battery systems, most parameters for the positive electrode active material and electrolyte solution used in the simulations were obtained from the COMSOL battery design module library based on the values for $Li(Ni_{0.33}Mn_{0.33}Co_{0.33})O_2$ and $LiPF_6$ in EC: DEC 1:1, respectively. It should be noted that the active material of the positive electrode and the electrolyte parameters used in the simulation may differ from the materials typically used in RMBs. Despite these differences, this study primarily aims to investigate the qualitative influence of morphological features and transport parameters (e.g. diffusion coefficient and current density) on Mg electrodeposition. The qualitative trends discussed in this study are expected to be applicable to different material systems.

However, the following important parameters were experimentally determined based on our previous report [30]: the relationship between the open-circuit voltage (OCV) and the state of charge (SOC) was determined from the discharge-charge curve with α-K_xMnO_2 in 0.5 mol dm^{-3} $[Mg(G4)][TFSA]_2$ dissolved in [Pyr1,3][TFSA] (G4: tetraglyme, TFSA: bis(trifuoromethanesulfonyl)-amide, [Pyr1,3][TFSA]: N-methyl-N-propylpyrrolidinium TFSA) at 100°C. Note that RMBs currently demonstrate more stable and consistent performance at elevated temperatures using oxide-based positive electrode active materials [11,12,30], whereas achieving adequate performance at room temperature remains challenging. The diffusion coefficient in the positive electrode active material was set to 1×10^{-15} m^2 s^{-1}, which was 1–2 orders smaller than that in $Li(Ni_{0.33}Mn_{0.33}Co_{0.33})O_2$. It should be noted that SOC was set to 1 at the capacity of 200 mAh g^{-1}.

To simulate the electrodeposition of Mg on the pits formed on the Mg metal negative electrode due to dissolution during discharge, a well-type structure with a width, length and depth of 50, 55 μm, and 25 μm, respectively, was constructed to model a pit as shown in Fig. 1. Table 1

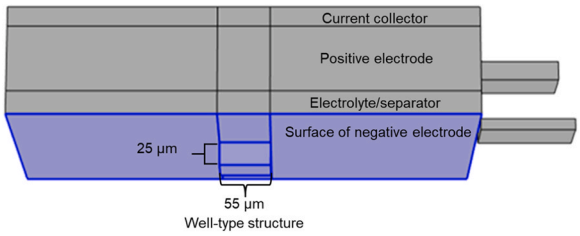

Fig. 1. 3D model of the cell structure used for the simulations. The thickness of the cell is magnified by a factor of 200 for clarity.

Table 1
Parameter values used in the modelling.

Parameters	Negative electrode	Separator	Positive electrode
Thickness (μm)	–	25	70
Particle radius (μm)	–	–	2
Initial electrolyte concentration, c_0 (mol m^{-3})	–	500	–
Max Mg^{2+} ion concentration, c_{max} (mol m^{-3})	49000	–	–
Porosity, ε	–	0.4	0.35
Diffusion coefficient in the active material of the positive electrode, D_s (cm^2 s^{-1})	–	–	1×10^{-15}
Charge transfer coefficient, α_c	0.5	–	–
Charge transfer coefficient, α_a	0.5	–	–
Rate constant, k (m s^{-1})	–	–	2×10^{-11}
Conductivity of electrolyte, σ (mS cm^{-1})	–	1.147	–
Transference number of cation, t_+^0	–	0.26	–
Exchange current density, i_0 (A m^{-2})	0.1	–	–
Mean molar activity coefficient, f_{+-}	–	0.13	–

lists the cell configuration parameters used in the model. The thicknesses of the current collector, positive electrode and separator, were 21, 75 and 25 μm, respectively. The surface of the Mg negative electrode is defined as the surface of the cell structure, and the negative electrode thickness is not considered. Fig. 2 shows the simulated charge curves for the C-rates of 1 C and 3 C with a cutoff voltage of 2.2 V at 293.15 K. The voltage plateaus are observed at 1.8–2 V and a rapid increase in the voltage was observed in the subsequent charging, indicating that the simulation results at these conditions are reasonable.

The Mg electrode samples for experimental validation were prepared by galvanostatic dissolution-deposition. Mg disks (99.99 %, $t = 40$ μm, φ = 16 mm) were polished mechanically with sand paper inside the Ar-filled glove box (O_2, H_2O <0.1 ppm), washed with dimethoxyethane to remove remaining fine powders, and then dried under vacuum for

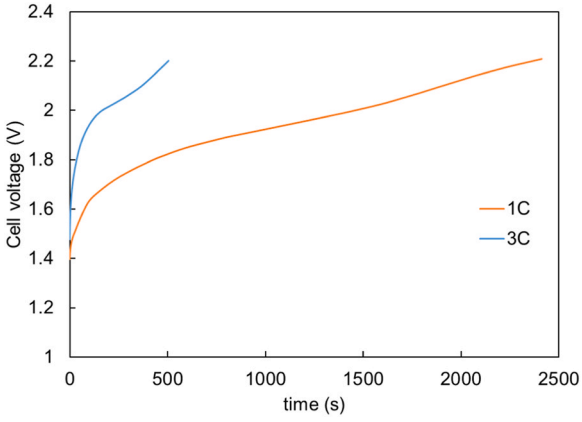

Fig. 2. Simulated charge curves at 1 C and 3 C with a cutoff voltage of 2.2 V.

30 min. Symmetric cells were fabricated using two sheets of polished Mg electrodes, Teflon ring as the spacer (ID = 14 mm, $t = 200$ μm), and 0.3 mol dm^{-3} $Mg[Al(HFIP)_4]_2$/G2 (HFIP: hexafluoro-iso-propoxyl group, G2: diglyme) as the electrolyte. The electrolyte was synthesized using a previously reported method [31]. Galvanostatic cycling measurements were conducted using an automatic charge-discharge instrument (HJ0610SD8C, Hokuto-Denko Co., Ltd.). The electrodes were first anodically dissolved at a fixed current density of 1 mA cm^{-2}, and then re-deposited on the same electrodes at the various current densities in the 0.01–20 mA cm^{-2} range. The areal capacities for both dissolution and deposition were fixed at 1 mAh cm^{-2}. The processed electrodes were retrieved from the cycled cells in a glove box, washed with dimethoxyethane, vacuum-dried, and then observed by scanning electron microscopy (SEM; JSM-7800F, JEOL) without any exposure to air by carry out the employing a designated airtight chamber.

4. Results and discussion

4.1. Simulation of rechargeable Mg battery

To develop a strategy for achieving uniform Mg electrodeposition, a 3D cell model, as shown in Fig. 1, was constructed to obtain the concentration distribution and flux of Mg^{2+} ions in the electrolyte solution and the current density during charging. Fig. 3a shows a cross-sectional view of the time-dependent changes in the concentration distribution of the Mg^{2+} ions in the cell. During charging, Mg metal was deposited on the negative electrode including in the area within the well-type structure. The concentration of Mg^{2+} ions decreased with time, and the degree of decrease was greater in the well-type structure than outside the well-type structure. This is because in the well-type structure, a unit volume of the electrolyte solution is surrounded to a greater extent by the Mg negative electrode, so that the consumption of Mg^{2+} ions is higher while the supply of Mg^{2+} ions is lower. As observed from the more detailed profiles of the Mg^{2+} ion concentration at different times shown in Fig. 3b, the concentration decreased significantly within approximately 60 s after the start of charging and then remained constant, suggesting a steady state. On the other hand, surprisingly, a slight increase in the concentration of the Mg^{2+} ions is observed in the electrolyte solution soaked into the composite positive electrode. This is because the Mg^{2+} ions extracted from the composite positive electrode did not diffuse sufficiently due to their low diffusion coefficients. Fig. 3c shows that the Mg^{2+} ion flux changes with time near the well-type structure, and the flux increases on the surface of the negative electrode. Up to approximately 60 s after the beginning of charging, the flux inside the well-type structure was greater than that outside the structure, and the concentration inside the well-type structure decreased. In addition, flux vectors toward the surrounding Mg negative electrode were observed inside the well-type structure, indicating that the flow of Mg^{2+} ions was altered by the surface structure of the negative electrode. Fig. 3d shows the current-density distribution on the surface of the Mg metal negative electrode at four different times. As shown in the figure, the surface cathodic current density, which is negative, is shifted to more

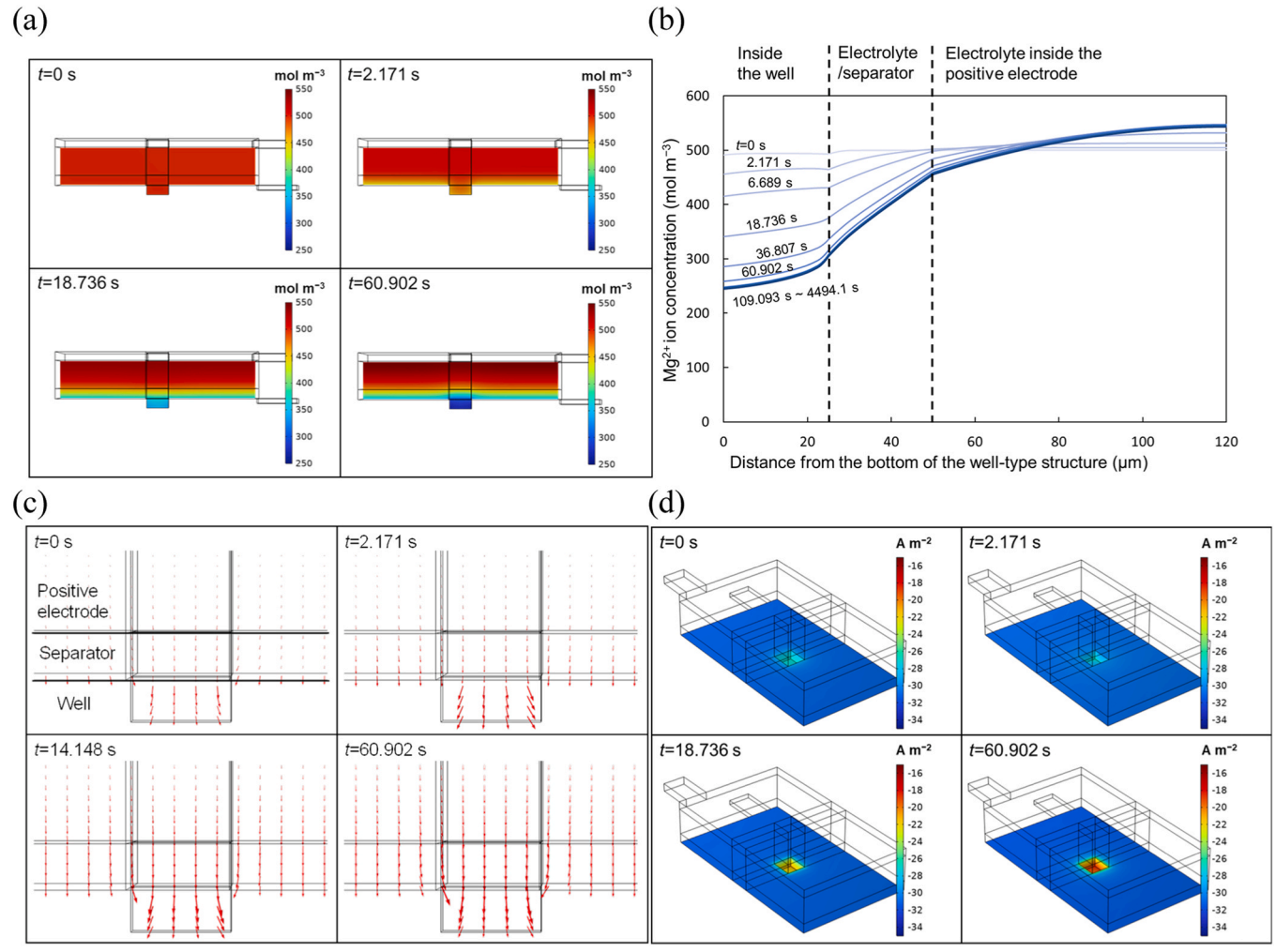

Fig. 3. (a) Distribution of Mg^{2+} ion concentration at four different times, (b) dynamic changes in the Mg^{2+} ion concentration as a function of the distance from the bottom of the well-type structure, (c) Mg^{2+} ion flux vectors, and (d) current density distribution on the Mg negative electrode surface upon 1 C charging.

positive values in the well-type structure compared to the outside of the well-type structure in few tens of seconds, corresponding to the lack of Mg^{2+} ions in the well-type structure observed in Fig. 3a. Because the current density is directly related to the amount of Mg electrodeposition, these results indicate that Mg electrodeposition is suppressed inside the well-type structure compared to outside the well-type structure, at least after reaching a steady state. Therefore, it is suggested that avoiding a decrease in the concentration of Mg^{2+} ions inside the well-type structure is essential for suppressing nonuniform electrodeposition. The concentrations of Mg^{2+} ions inside and outside the well-type structure were investigated by varying the diffusion coefficient of Mg^{2+} ions in the electrolyte solution, the size of the well-type structure, the initial concentration of Mg^{2+} ions within the well-type structure, and the C-rate. Three different positions in the cell structure were selected as representative points, as shown in Fig. 4, to observe the concentration changes over time in detail. Position 1 is located at the bottom of the well-type structure, position 2 is located at the entrance of the well-type structure, and position 3 is located at the interface between the positive electrode and the separator. Fig. 5 shows the Mg^{2+} ion concentra

tion at the three positions after charging up to 2.2 V, for each value of the diffusion coefficient of Mg^{2+} ions in the electrolyte solution and the volume of the well-type structure. One of the advantages of modeling is that the influence of the Mg^{2+} ion diffusion coefficient on Mg electrodeposition can be easily investigated, whereas this is significantly more difficult to examine experimentally. At the lowest value of the diffusion coefficient (7.5×10^{-11} m^2 s^{-1}), the concentration at position 1, *i.e.* the bottom of the well-type structure, decreases to 500 mol m^{-3} which is less than half of the initial value. A similar concentration drop was observed at positions 2 and 3; however, the magnitude of the decrease became smaller as the position approached the positive electrode. A larger volume of the well-type structure lowers the magnitude of the decrease in the Mg^{2+} concentration; however, the volume increase of the well-type structure does not completely eliminate the concentration change. These results show that a concentration gradient is formed in the cell in the direction perpendicular to the Mg negative electrode for the lower values of the Mg^{2+} coefficient of diffusion in the electrolyte solution. On the other hand, at the Mg^{2+} diffusion coefficient of 7.5×10^{-9} m^2 s^{-1}, the ion concentration after charging remains almost unchanged compared to the initial concentration, regardless of the position, and an evident concentration gradient is not formed within the cell. Therefore, it is suggested that an increase in the diffusion coefficient of Mg^{2+} ions in the electrolyte solution can effectively suppress the concentration gradient and the nonuniform electrodeposition.

Next, we modeled the case when charging began immediately after discharging and the dissolved Mg^{2+} ions had not yet diffused sufficiently far from the inside of the well-type structure. Fig. 6 shows the time dependence of the Mg^{2+} ion concentration and the Mg^{2+} ion flux vector. In the early stages of charging, within 1.3464 s, the Mg^{2+} ion concentration in the well-type structure was higher than that in the electrolyte solution, and the ions diffused toward the positive electrode owing to the concentration gradient. After 16.786 s, the concentration in the well-type structure became lower than that in the electrolyte solution, and a similar steady-state flux toward the Mg negative electrode (Fig. 3c) was observed, indicating that the concentration distribution in the initial state became homogeneous after tens of seconds. Therefore, to utilize the high concentration of Mg^{2+} ions in a well-type structure, the battery should be charged immediately after discharging.

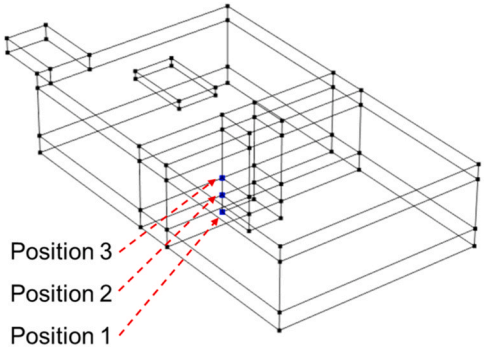

Fig. 4. Schematic diagram showing positions 1, 2, and 3 in the cell structure.

Fig. 7 shows the concentration changes in the homogeneous electrolyte solution at 0.5 C and 2 C, which indicate that the concentration of Mg^{2+} ions inside the well-type structure decreases more strongly for higher C-rates. This is due to the higher rate of Mg^{2+} ion consumption at higher C rates. Thus, a lower C-rate was favorable for maintaining a steady Mg^{2+} ion concentration in the well-type structure, leading to homogeneous Mg deposition.

These results suggest that the Mg^{2+} ion concentration within the well-type structure is determined by three factors: (1) the initial ion concentration, (2) the rate of ion supply, determined by the diffusion coefficient and depth of the well-type structure, and (3) the rate of ion consumption, determined by the current density during charging. Therefore, maintaining a homogeneous Mg^{2+} ion concentration distribution is crucial for preventing nonuniform Mg electrodeposition. In the Supporting Information, based on the above results, a dimensionless number *A* is proposed to characterize the homogeneity of the Mg^{2+} ion concentration with a higher *A* value guaranteeing lower variation of the Mg^{2+} ion concentration in the cell.

4.2. Electrodeposition on Mg negative electrode

Electrodeposition on a non-uniform Mg metal surface was experimentally conducted with current densities varying from 0.01 to 20 mA cm^{-2}. The Mg metal electrode with a nonuniform surface was obtained by anodic polarization at 1 mA cm^{-2} in the $Mg[Al(HFIP)_4]_2$/G2 electrolyte used as a representative non-corrosive electrolyte for 1 h at room temperature. While traditional RMB electrolytes often contain chloride ions, this study employed a chloride-free electrolyte system to prevent the electrode corrosion, which is a problem associated with chloride-containing electrolytes as reported by Yagi et al. [32]. Fig. 8a show the SEM images of the Mg metal negative electrodes before and after the electrodeposition at 0.01–20 mA cm^{-2} at a fixed areal capacity of 1 mAh cm^{-2}. As shown in Fig. 8a, the Mg metal surface before electrodeposition displays multiple pits. It is also observed that electrodeposition occurred mainly on the fringe of the pits for current densities above 1 mA cm^{-2}, as reported in previous studies [33,34]. Conversely, at the current density of 0.01 mA cm^{-2}, electrodeposition occurred more homogeneously including within the pits. To quantitatively evaluate the uniformity of Mg electrodeposition, the fraction of the area of Mg metal locally deposited outside the dissolution pits was calculated from the SEM images shown in Fig. 8a using ImageJ software (Fig. 8b). In the low current density region, the fraction increases with increasing the current density up to 3 mA cm^{-2} and then gradually decreases with increasing the current density above 8 mA cm^{-2}. The reason of this behavior is possibly because of the change in the morphology of electrodeposited Mg; island-like deposition of Mg was observed at 10–20 mA cm^{-2}, while the deposited Mg was relatively flat at 1–8 mA cm^{-2}. As shown in the simulation result in Fig. 3a upon 1 C (3.137 mA cm^{-2}) charging, the Mg^{2+} concentration in the dissolution pits was significantly lowered, which leads to the suppression of the current density in the dissolution pits as can be seen in Fig. 3d. In contrast, in the simulation result at 0.5 C (1.5685 mA cm^{-2}) in Fig. 7a, the concentration depletion was mitigated compared to the result at 1 C. As discussed above, both the experimental and simulation results suggest that lowering the Mg^{2+} ion consumption inside the pits at a lower current density reduces the difference in the electrodeposition between the outside and inside the pits.

Consequently, reduction of the current density and suppression of ion consumption within the pits are effective strategies for promoting

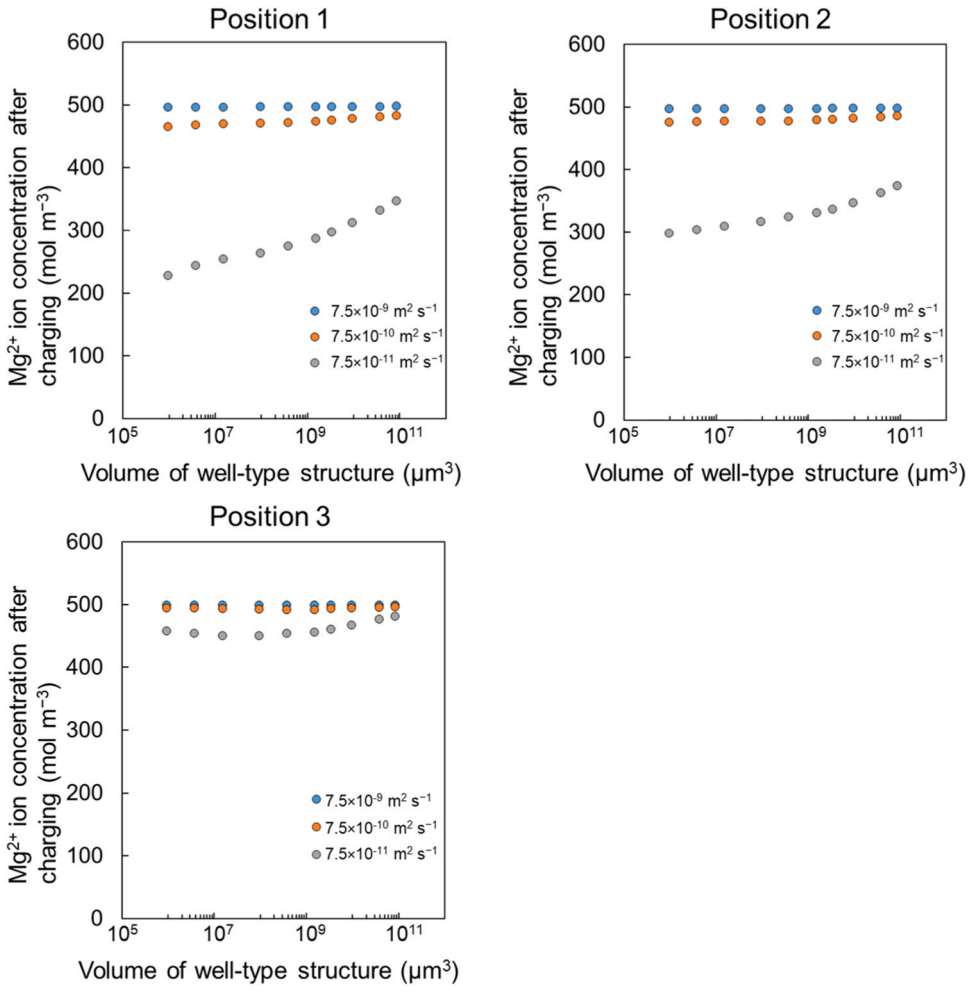

Fig. 5. Mg^{2+} ion concentration after charging up to 2.2 V and volume of the well-type structure at positions 1, 2, and 3. The diffusion coefficient was varied from 7.5×10^{-11} to 7.5×10^{-9} m^2 s^{-1}, and the volume was varied from 9.4×10^5 to 8.4×10^{10} μm^3 by multiplying the width and length by a constant without changing the depth.

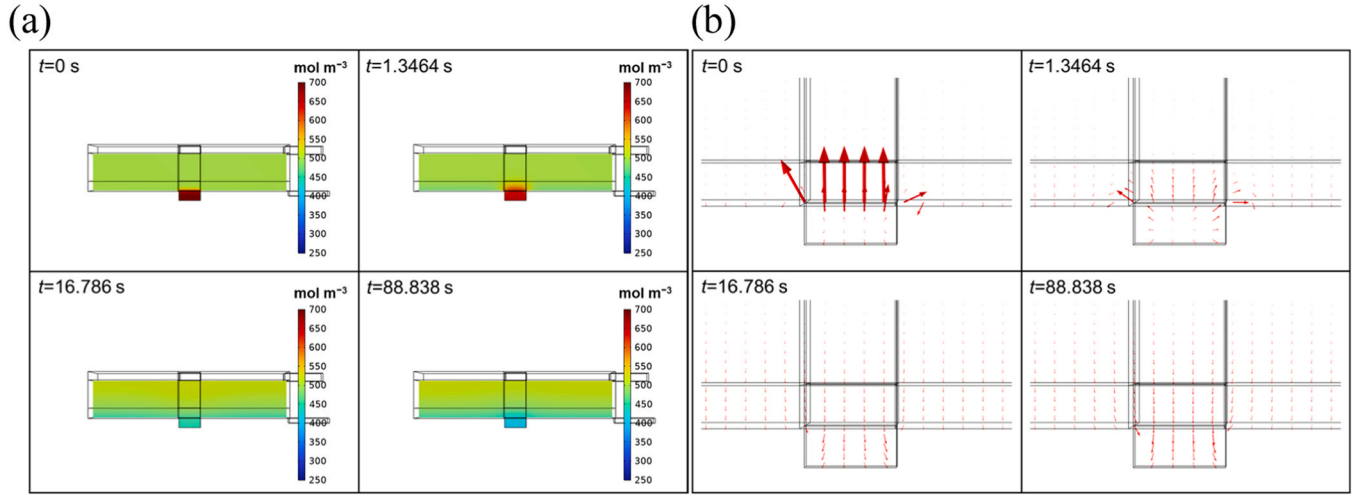

Fig. 6. Time dependence of (a) Mg^{2+} ion concentration and (b) Mg^{2+} ion flux during charging when the concentration inside the well-type structure is higher (700 mol m^{-3}) than the surrounding area (500 mol m^{-3}) at the diffusion coefficient of 7.5×10^{-11} m^2 s^{-1}.

electrodeposition inside the pits. Furthermore, increasing the Mg^{2+} ion diffusion coefficient in the electrolyte solution to enhance the ion supply within the pit is a promising approach for filling the pits.

5. Conclusions

Simulations of rechargeable Mg batteries were conducted to

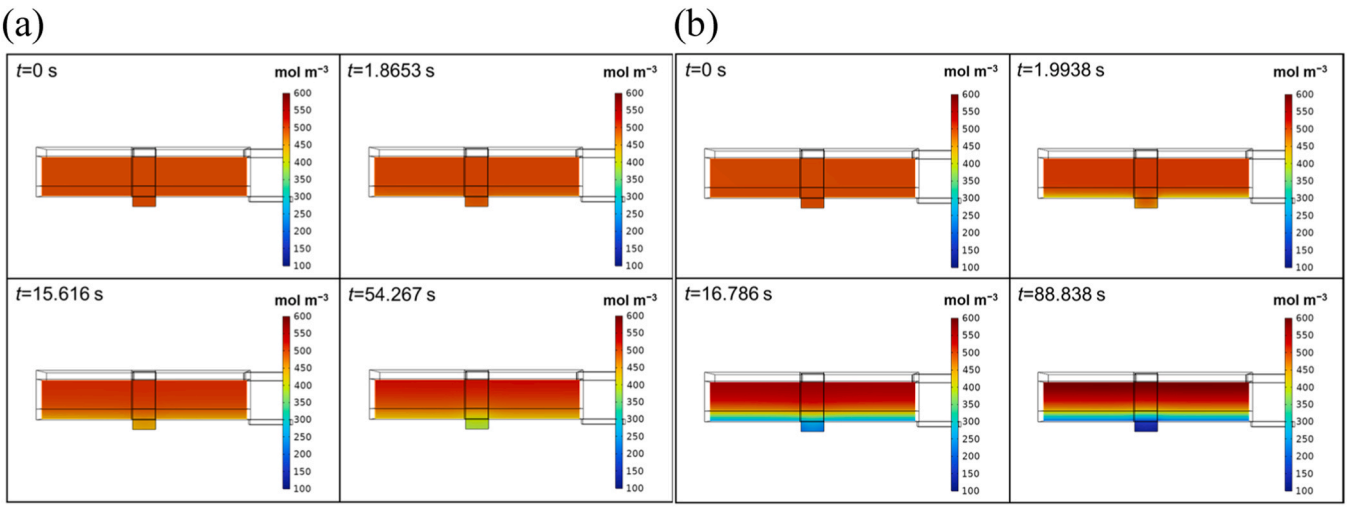

Fig. 7. Time dependence of the changes of the Mg^{2+} ion concentration distribution for C rates of (a) 0.5 C and (b) 2 C for the diffusion coefficient of 7.5×10^{-11} m^2 s^{-1}.

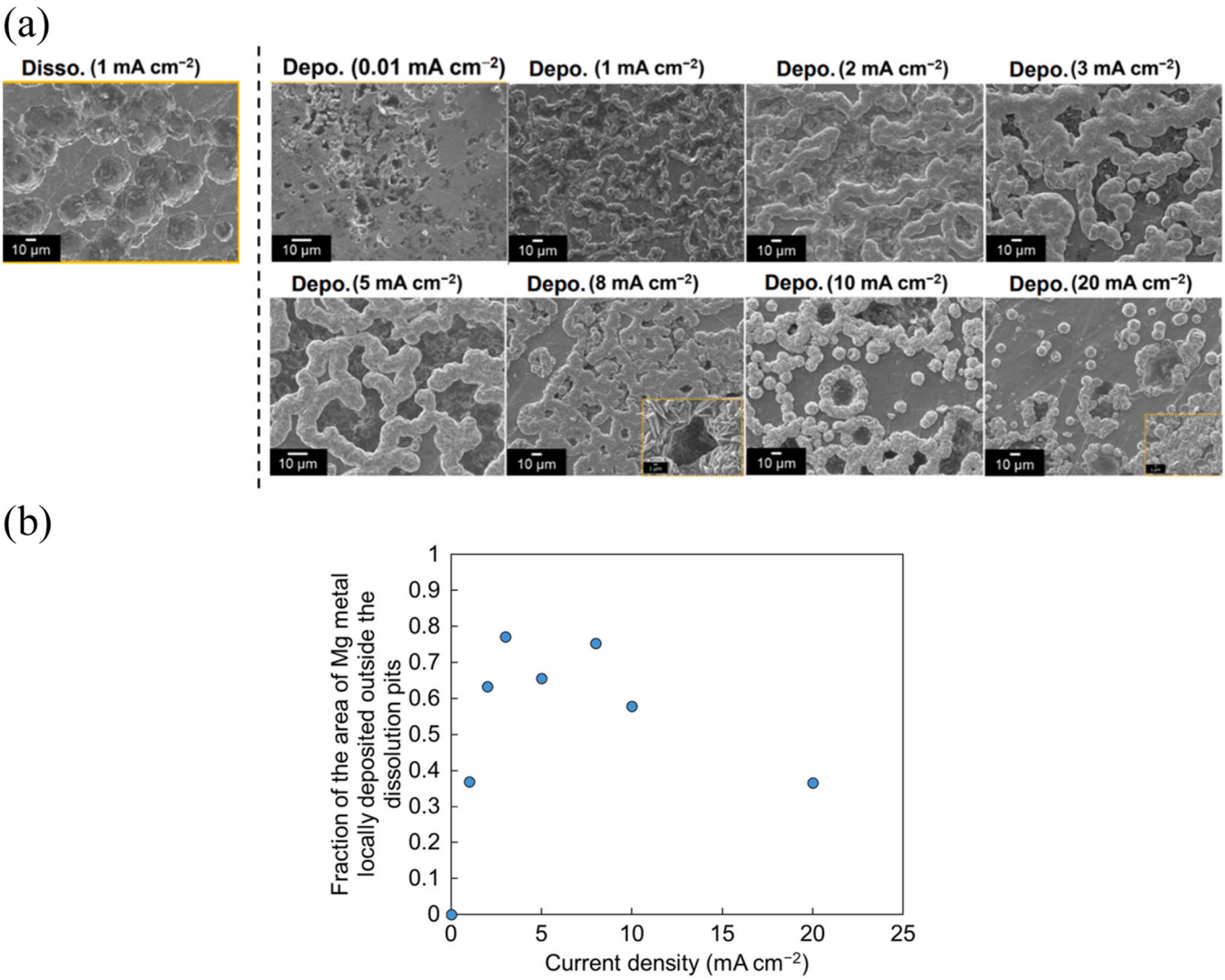

Fig. 8. (a) SEM images of the surface of Mg metal negative electrode dissolved at 1 mA cm^{-2} (left-hand side) and the surface of the Mg negative electrode with Mg metal deposited at various current densities (right-hand side). (b) Current density dependence of fraction of the area of Mg metal locally deposited outside the dissolution pits estimated by SEM images of (a).

investigate the distribution of Mg deposition on a Mg metal negative electrode containing pits formed by dissolution during discharge. While simulations have been rarely used in previous work on rechargeable Mg batteries, Newman model, which is commonly used for LIBs, was successfully applied in this study. The surface morphology of the Mg metal negative electrode affects the distribution of Mg^{2+} ions, flux, and current density, leading to non-uniform Mg electrodeposition which negatively affects battery performance. To solve this problem, simulations and experiments have shown that either the diffusion coefficient of Mg^{2+} ions in the electrolyte must be increased to 7.5×10^{-9} or higher or the current density must be maintained at 0.01 or lower. Furthermore, a dimensionless number *A* is proposed in supporting information.

Future simulations of RMBs should incorporate experimental data for the transport characteristics of the electrolytes and positive electrode materials. Our simulation results demonstrate that Mg metal electrodeposition on the fringes of the pits becomes more pronounced at high current densities, but is suppressed at low current densities, in agreement with the experimental observations.

CRediT authorship contribution statement

Toshihiko Mandai: Validation, Investigation. **Atsushi Tamura:** Writing – original draft, Visualization, Software, Methodology, Investigation, Formal analysis, Conceptualization. **Shunsuke Yagi:** Writing – review & editing, Supervision, Resources, Project administration, Formal analysis, Conceptualization.

Declaration of Competing Interest

The authors declare that they have no known competing financial interests or personal relationships that could have appeared to influence the work reported in this paper.

Acknowledgements

This study was supported by the Japan Science and Technology Agency (JST) GteX Program (Grant Number: JPMJGX23S1) and the Japan Society for the Promotion of Science (JSPS: 23H01738, 23H05452, and 23K17812). The authors thank Prof. Tetsu Ichitsubo of Tohoku University for his valuable advice, particularly regarding dimensionless number.

Appendix A. Supporting information

Supplementary data associated with this article can be found in the online version at doi:10.1016/j.mtcomm.2025.113325.

Data availability

Data will be made available on request.

References

[1] X.B. Cheng, R. Zhang, C.Z. Zhao, Q. Zhang, Toward safe lithium metal anode in rechargeable batteries: a review, Chem. Rev. 117 (15) (2017) 10403–10473, https://doi.org/10.1021/acs.chemrev.7b00115.
[2] J.M. Tarascon, M. Armand, Issues and challenges facing rechargeable lithium batteries, Nature 414 (2001) 359–367, https://doi.org/10.1021/acs.chemrev.7b00115.
[3] A. Das, N.T.M. Balakrishnan, P. Sreeram, M.J.J. Fatima, J.D. Joyner, V.K. Thakur, A. Pullanchiyodan, J.H. Ahn, P. Raghavan, Prospects for magnesium ion batteries: a comprehensive materials review, Coord. Chem. Rev. 502 (2024) 215593, https://doi.org/10.1016/j.ccr.2023.215593.
[4] D. Wang, Z. Zhang, Y. Hao, H. Jia, X. Shen, B. Qu, G. Huang, X. Zhou, J. Wang, C. Xu, F. Pan, Challenges and progress in rechargeable magnesium-ion batteries: materials, inter-faces, and devices, Adv. Funct. Mater. 34 (2024) 2410406, https://doi.org/10.1002/adfm.202410406.
[5] M. Matsui, Study on electrochemically deposited Mg metal, J. Power Sources 196 (16) (2011) 7048–7055, https://doi.org/10.1016/j.jpowsour.2010.11.141.
[6] G. Wang, Z. Wang, H. Shi, A. Du, M. Sun, G. Cui, Progress and perspective on rechargeable magnesium-ion batteries, Sci. China Press 67 (1) (2024) 214–246, https://doi.org/10.1007/s11426-022-1454-0.
[7] J. Zhang, Z. Chang, Z. Zhang, A. Du, S. Dong, Z. Li, G. Li, G. Cui, Current design strategies for rechargeable magnesium-based batteries, ACS Nano 15 (2021) 15594–15624, https://doi.org/10.1021/acsnano.1c06530.
[8] D. Aurbach, Z. Lu, A. Schechter, Y. Gofer, H. Gizbar, R. Turgeman, Y. Cohen, M. Moshko-vich, E. Levi, Prototype systems for rechargeable magnesium batteries, Nature 407 (6805) (2000) 724–727, https://doi.org/10.1038/3503755.
[9] D. Muthuraj, S. Mitra, Reversible Mg insertion into chevrel phase Mo6S8 cathode: preparation, electrochemistry and X-ray photoelectron spectroscopy study, Mater. Res. Bull. 101 (2018) 167–174, https://doi.org/10.1016/j.materresbull.2018.01.031.
[10] J. Han, S. Yagi, H. Takeuchi, M. Nakayama, T. Ichitsubo, Catalytic mechanism of spinel oxides for oxidative electrolyte decomposition in Mg rechargeable batteries, J. Mater. Chem. A Mater. 9 (46) (2021) 26401–26409, https://doi.org/10.1039/d1ta08115b.
[11] S. Okamoto, T. Ichitsubo, T. Kawaguchi, Y. Kumagai, F. Oba, S. Yagi, K. Shimokawa, N. Goto, T. Doi, E. Matsubara, Intercalation and push-out process with spinel-to-rocksalt transition on Mg insertion into spinel oxides in magnesium batteries, Adv. Sci. 2 (8) (2015) 1500072, https://doi.org/10.1002/advs.201500072.
[12] T. Hatakeyama, N.L. Okamoto, K. Shimokawa, H. Li, T. Kawaguchi, A. Nakao, Y. Uchimoto, H. Tanimura, T. Ichitsubo, Electrochemical phase transformation accompanied with Mg ex-traction and insertion in a spinel $MgMn_2O_4$ cathode material, Phys. Chem. Chem. Phys. 21 (42) (2019) 23749–23757, https://doi.org/10.1039/c9cp04461b.
[13] J. Heath, H. Chen, M.S. Islam, $MgFeSiO_4$ as a potential cathode material for magnesium batteries: Ion diffusion rates and voltage trends, J. Mater. Chem. A Mater. 5 (25) (2017) 13161–13167, https://doi.org/10.1039/c7ta03201c.
[14] T. Hatakeyama, H. Li, N.L. Okamoto, K. Shimokawa, T. Kawaguchi, H. Tanimura, S. Imashuku, M. Fichtner, T. Ichitsubo, Accelerated kinetics revealing metastable pathways of magnesiation-induced transformations in MnO_2 polymorphs, Chem. Mater. 33 (17) (2021) 6983–6996, https://doi.org/10.1021/acs.chemmater.1c02011.
[15] V. Goel, K. Thornton, Enabling the electrochemical simulation of Li-ion battery electrodes with anisotropic tortuosity in COMSOL Multiphysics®, MethodsX 8 (2021) 101425 https://doi.org/10.1016/j.mex.2021.101425.
[16] Y. Takagishi, Y. Tozuka, T. Yamanaka, T. Yamaue, Heating simulation of a Li-ion battery cylindrical cell and module with consideration of gas ejection, Energy Rep. 8 (2022) 3176–3188, https://doi.org/10.1016/j.egyr.2022.02.086.
[17] G. Bai, P. Wang, An internal state variable mapping approach for Li-Plating diagnosis, J. Power Sources 323 (2016) 115–124, https://doi.org/10.1016/j.jpowsour.2016.05.040.
[18] H.K. Bergstrom, K.D. Fong, B.D. McCloskey, Interfacial effects on transport coefficient measurements in Li-ion battery electrolytes, J. Electrochem Soc. 168 (6) (2021) 060543, https://doi.org/10.1149/1945-7111/ac0994.
[19] P. Singh, N. Khare, P.K. Chaturvedi, Li-ion battery ageing model parameter: SEI layer analysis using magnetic field probing, Eng. Sci. Technol. 21 (1) (2018) 35–42, https://doi.org/10.1016/j.jestch.2018.01.007.
[20] M. Doyle, Y. Fuentes, Computer simulations of a lithium-ion polymer battery and implications for higher capacity next-generation battery designs, J. Electrochem. Soc. 150 (6) (2003) A706, https://doi.org/10.1149/1.1569478.
[21] M. Doyle, J. Newman, A.S. Gozdz, C.N. Schmutz, J.M. Tarascon, Comparison of modeling predictions with experimental data from plastic lithium ion cells, acknowledgment, J. Electrochem. Soc. 143 (6) (1996) 1890, https://doi.org/10.1149/1.1836921.
[22] K. Kumaresan, G. Sikha, R.E. White, Thermal model for a Li-ion cell, J. Electrochem. Soc. 155 (2) (2008) A164, https://doi.org/10.1149/1.2817888.
[23] S.U. Kim, B. Perdue, C.A. Apblett, V. Srinivasan, Understanding performance limitations to enable high performance magnesium-ion batteries, J. Electrochem. Soc. 163 (8) (2016) A1535–A1542, https://doi.org/10.1149/2.0321608jes.
[24] R. Krishna, J.A. Wesselingh, The Maxwell-Stefan approach to mass transfer, Chem. Eng. Sci. 52 (6) (1997) 861–911, https://doi.org/10.1016/S0009-2509(96)00458-7.
[25] J. Newman, K.E. Thomas-Alyea. Electrochemical Systems, Third edition, John Wiley & Sons, Inc, Hoboken, New Jersey, 2004.
[26] T.F. Fuller, M. Doyle, J. Newman, Simulation and optimization of the dual lithium ion insertion cell, J. Electrochem. Soc. 141 (1) (1994) 1, https://doi.org/10.1149/1.2054684.
[27] Richard Alkire, Brian Gracon, Flow-through porous electrodes, J. Electrochem. Soc. 122 (12) (1975) 1594, https://doi.org/10.1149/1.2134076.
[28] P. Arora, M. Doyle, A.S. Gozdz, R.E. White, J. Newman, Comparison between computer simulations and experimental data for high-rate discharges of plastic lithium-ion batteries, J. Power Sources 88 (2) (2000) 219–231.
[29] J. Newman, T.W. Chapman, Restricted diffusion in binary solutions, AIChE J. 19 (2) (1973) 343–348, https://doi.org/10.1002/aic.690190220.
[30] I. Oda-Bayliss, S. Yagi, M. Kamiko, K. Shimada, H. Kobayashi, T. Ichitsubo, Effect of vanadium doping on α-$KxMnO_2$ as a positive electrode active material for rechargeable magnesium batteries, J. Mater. Chem. A Mater. 12 (28) (2024) 17510–17519, https://doi.org/10.1039/d4ta00659c.
[31] T. Mandai, Y. Youn, Y. Tateyama, Remarkable electrochemical and ion-transport characteristics of magnesium-fluorinated alkoxyaluminate-diglyme electrolytes for magnesium batteries, Mater. Adv. 2 (19) (2021) 6283–6296, https://doi.org/10.1039/d1ma00448d.

[32] S. Yagi, A. Tanaka, Y. Ichikawa, T. Ichitsubo, E. Matsubara, Electrochemical stability of magnesium battery current collectors in a grignard reagent-based electrolyte, J. Electrochem. Soc. 160 (3) (2013) C83–C88, https://doi.org/10.1149/2.033303jes.

[33] T. Mandai, H. Somekawa, Ultrathin magnesium metal anode – an essential component for high-energy-density magnesium battery materialization, Batter Supercaps 5 (9) (2022) e202200153, https://doi.org/10.1002/batt.202200153.

[34] X. Liu, A. Du, Z. Guo, C. Wang, X. Zhou, J. Zhao, F. Sun, S. Dong, Guanglei Cui, Uneven stripping behavior, an unheeded killer of Mg anodes, Adv. Mater. 34 (31) (2022) 2201886, https://doi.org/10.1002/adma.202201886.